

LB**M**amba: Locally Bi-directional Mamba

Jingwei Zhang*

Department of Computer Science, Stony Brook University, Stony Brook, NY, USA

Xi Han*

Department of Computer Science, Stony Brook University, Stony Brook, NY, USA

Hong Qin

Department of Computer Science, Stony Brook University, Stony Brook, NY, USA

Mahdi S. Hosseini

Concordia University, Montreal, Canada

Mila–Quebec AI Institute, Montreal, Canada

Dimitris Samaras

Department of Computer Science, Stony Brook University, Stony Brook, NY, USA

jingweizhang@cs.stonybrook.edu

xihan1@cs.stonybrook.edu

qin@cs.stonybrook.edu

mahdi.hosseini@concordia.ca

samaras@cs.stonybrook.edu

Abstract

Mamba, a State Space Model (SSM) that accelerates training by recasting recurrence as a parallel selective scan, has recently emerged as a linearly-scaling, efficient alternative to self-attention. Because of its unidirectional nature, each state in Mamba only has information of its previous states and is blind to states after. Current Mamba-based computer-vision methods typically overcome this limitation by augmenting Mamba’s global forward scan with a global backward scan, forming a bi-directional scan that restores a full receptive field. However, this operation doubles the computational load, eroding much of the efficiency advantage that originally Mamba have. To eliminate this extra scans, we introduce **LB**M**amba**, a locally bi-directional SSM block that embeds a lightweight locally backward scan inside the forward selective scan and executes it entirely in per-thread registers. Building on LB**M**amba, we present **LB**V**im**, a scalable vision backbone that alternates scan directions every two layers to recover a global receptive field without extra backward sweeps. We validate the versatility of our approach on both natural images and whole slide images (WSIs). We show that our LB**V**im constantly offers a superior performance–throughput trade-off. That is under the same throughput, LB**V**im achieves 0.8% to 1.6% higher top-1 accuracy on the ImageNet-1K classification dataset, 0.6% to 2.7 % higher mIoU on the ADE20K semantic segmentation dataset, 0.9% higher AP^b and 1.1% higher AP^m on the COCO detection dataset. We also integrate LB**M**amba into the SOTA pathology multiple instance learning (MIL) approach, MambaMIL, which uses single directional scan. Experiments on 3 public WSI classification datasets for show that our method achieves a relative improvement of up to 3.06% better AUC, 3.39% better F1, 1.67% better accuracy.

1 Introduction

State-space models (SSMs) have emerged as a compelling alternative to self-attention for sequence modeling because their hidden-state recurrence yields linear time and memory complexity with respect to sequence length (Gu et al., 2021a; Wang et al., 2022). Yet, conventional SSMs trained with naïve recurrence is still limited by slow training and inference, as they cannot leverage efficient parallelism of modern GPUs (Baron et al., 2023). Mamba (Gu & Dao, 2023) overcomes this by decoupling the state update from the hidden-to-output convolution and reformulating the computation as a selective parallel scan that runs efficiently on modern GPUs. Consequently, Mamba matches Transformer-level accuracy on long-range tasks while exhibiting far better resolution wise scaling characteristics, making it an attractive choice for both research and production systems. It was first introduced for natural-language processing and has since been

*These authors contributed equally to this paper.

adapted to computer vision (Zhu et al., 2024; Liu et al., 2024; Huang et al., 2024). Vision models built on Mamba’s selective-scan kernel delivers substantial GPU speed-ups and memory savings while consistently outperforming Transformer based baselines.

Standard computer vision mamba based models scan images multiple times from different directions to enhance their performance (Zhu et al., 2024; Liu et al., 2024; Yang et al., 2024a). There are two causes of such multiple scans: the first one is to overcome the 1D nature of Mamba. Mamba treats an image as a flattened 1D sequence, so a single left-to-right pass captures only row-wise context. To recover vertical dependencies, vision pipelines typically perform an additional scan on the column-wise ordering of patches, yielding two orthogonal sweeps that together approximate 2D spatial relationship (Liu et al., 2024; Yang et al., 2024a). Several dedicated 2D Mamba/SSM methods have recently been proposed to address this structural mismatch more directly (Zhang et al., 2024; Wang et al., 2024). The second issue is the unidirectional nature of SSMs: the latent state at position t is conditioned only on past positions $1 \dots t$ (Gu & Dao, 2023). Consequently, the model is blind to information occurring after position t , which often leads to sub-optimal performance on vision tasks. A common solution is to add a reverse (right-to-left or bottom-to-top) pass to restore access to future tokens, producing a bi-directional scan mechanism (Zhu et al., 2024). Although this strategy re-establishes a full receptive field, each extra sweep roughly doubles the computational load, eroding much of the efficiency advantage that originally Mamba offered.

To eliminate this extra scans required bi-directional scan, we propose LBMamba, a locally bi-directional SSM, together with the LBVim framework for vision tasks. Our main contributions are summarized below.

- We introduce a *local backward scan* and a *locally bi-directional SSM architecture* that integrates the backward update directly into Mamba’s forward scan, thereby eliminating the costly global backward scan and markedly improving computational efficiency.
- We propose a fast *hardware-aware thread-level bi-directional scanning operator* that performs the local backward scan entirely in thread-private registers, incurring *no* additional high-bandwidth memory traffic or inter-thread communication.
- We validate the speed (aka throughput)-accuracy trade-off of our architecture by implementing it on two very different domains: natural images and Giga-pixel Whole Slide Images (WSI).

We show that instead of conducting an extra backward scan, it is more beneficial to scale up the model size under a fixed latency budget. Experiments on natural images show that LBVim achieves better performance-throughput trade-off than the baselines. Under the same throughput, LBVim achieves 0.8% to 1.6% higher top-1 accuracy on the ImageNet-1K classification dataset, 0.6% to 2.7 % higher mIoU on the ADE20K semantic segmentation dataset, 0.9% higher AP^b and 1.1% higher AP^m on the COCO detection dataset. We also integrate our scanning approach into the SOTA pathology multiple instance learning (MIL) approach, MambaMIL ?. Extensive experiments on 3 public datasets for WSI classification and survival analysis datasets show that our method achieves a relative improvement of up to 3.06% better AUC, 3.39% better F1, 1.67% better accuracy.

2 Related work

State Space Model (SSM). SSM (Kalman, 1960) is an effective sequence model that represents systems evolving over time by defining hidden states and their transitions, which makes it particularly useful for capturing dynamic temporal behavior in sequential data. Gu et al. (2021b) unified RNNs, temporal convolutions, and neural differential equations with a linear state-space layer and demonstrated the potential of SSM-based models with the HiPPO initialization. Wang et al. (2022) proposed Bi-directional Gated SSM which is able to match BERT (Devlin et al., 2019) pretraining accuracy without attention. S4 (Gu et al., 2021a) normalized the parameter matrices into a diagonal structure and offered an option to use bi-directional convolution kernel. 2D-SSM (Baron et al., 2023) adopted a 2D-SSM recursion (Kung et al., 1977) and explored scanning image in two or four directions. Similarly, S4ND (Nguyen et al., 2022) extends S4 to images and videos by applying axis-wise updates successively along each spatial direction. Overall,

SSM architectures developed prior to Mamba were constrained by slow training efficiency because there lacks an efficient parallel algorithm.

Mamba. Mamba (Gu & Dao, 2023) proposed a selective mechanism that makes the model parameters input-dependent and thus allows remembering important states and discard less relevant ones, alleviating the forgetting in long sequences. It also introduced a hardware-aware parallel scan algorithm that drastically accelerates state computation. Hwang et al. (2024) proposed Hydra, a bi-directional Mamba model that using generalized matrix mixers and showed a better performance than BERT. Vim (Zhu et al., 2024) and VMamba (Liu et al., 2024) are the first two mamba based models in computer vision. Vim (Zhu et al., 2024) introduced a Vision Mamba block that uses two independent selective SSMs for bi-directional aggregation of information and achieves a global receipt field. VMamba (Liu et al., 2024) introduced a pyramid Mamba network with a 4-directional scan pattern to achieve a global receipt field and also enhance spatial understanding. It also proposed some solution to alleviate the instability issue in half precision training. PlainMamba (Yang et al., 2024a) also used a 4-directional selective scan and adopted a more spatially continuous scan path. 2DMmaba (Zhang et al., 2024) introduced a 2D SSM and extends Mamba’s parallel scan algorithm into this 2D SSM. It also use the 4-directional scan of VMamba in their natural image applications. For all of these 4-directional scans, they are all two groups of bi-directional scans applied on two different ordering of image patches. This bi-directional scan is now the standard approach in most mamba based vision models.

Application of Mamba in Whole Slide Images (WSI) analysis. WSIs are usually Giga-pixel images in the pathology domain. Most slides annotated only on slide level, requiring Multi Instance Learning (MIL) methods for WSI classification. It aggregates embedded features from a WSI for slide-level representation. MIL approaches are usually based on some attention mechanism (Ilse et al., 2018; Lu et al., 2021; Li et al., 2021) and self-attention mechanism (Shao et al., 2021). Recently, S4MIL (Fillioux et al., 2023) introduced S4 model to WSI analysis, which demonstrated the effectiveness of SSM in capturing long-range dependencies, but it does not utilize the parallel scan and thus slow. Yang et al. (Yang et al., 2024b) used Mamba and a sequence reordering mechanism to reduce overfitting and achieved even better performance. Note that these SSM based MIL methods does not use bi-directional scan.

3 Method

We first revisit the recursions used in Mamba and existing standard bi-directional formulations. Then we present LBMamba designed for efficiency, and an associated vision mamba framework: LBVim. Finally, we introduce the low-level CUDA design of LBMamba.

3.1 SSM in Mamba and existing standard bi-directional SSM

The original SSM in Mamba (Gu & Dao, 2023) is a mathematical model used to capture the behavior of continuous dynamic systems. To be integrated into deep models, it is discretized as:

$$h_t^f = \bar{A}^f h_{t-1}^f + \bar{B}^f x_t \quad (1)$$

$$y_t^f = C^f h_t^f + D^f x_t \quad (2)$$

where x_t is the input token, h_t^f is the latent state at time t , y_t^f is the output token, D is a parameter, C^f is the state dimension coefficient to aggregate N state dimensions into a single output and we use the superscript f to denote this is a forward scan instead of a backward one. In this paper, following previous conversion (Zhu et al., 2024), "forward" and "backward" represents the scan direction rather than the forward/backward propagation in neural network training. The parameters \bar{A}^f , \bar{B}^f and \bar{C}^f are functions of the input x_t , which allows the SSM to dynamically adapt to the input context (known as the selective mechanism (Gu & Dao, 2023)). This aggregates important input into the hidden state while unimportant input can be ignored. Mathematically, they are:

$$\bar{A}_t^f = \exp(\Delta_t A^f), \quad \bar{B}_t^f = \Delta_t B^f(x_t), \quad C_t^f = C^f(x_t), \quad \Delta_t = \text{softplus}(\Delta(x_t)) \quad (3)$$

where Δ , B^d , and C^d are learnable linear functions of x_t . Δ_t represents the time step of the discretization. The selective mechanism in the Mamba block is commonly referred to as a selective scan.

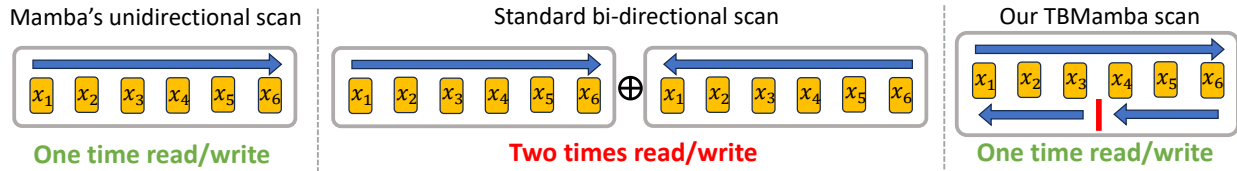


Figure 1: (Left): The unidirectional scanning mechanism of the vanilla Mamba (Gu & Dao, 2023), where each state only has information of its previous/left states. (Center): Standard bi-directional scanning mechanism (Zhu et al., 2024), where a dedicated backward scan is conducted and added to the forward scan. This operation involves an additional read/write of the data and thus doubles the running time. (Right): Our LBMamba scan conducts a locally backward scan which is integrated into the forward scan process. This involves only one time read/write operations and thus very fast.

From equation 1, we can find that the output y_t^f only contains information of its previous inputs $\{x_i | i < t\}$. It is also illustrated in figure 1 left. In order to enable a global recept field, previous approaches (Zhu et al., 2024; Liu et al., 2024; Yang et al., 2024a) commonly apply a backward scan and add them together as the output y_t (figure 1 center):

$$h_t^b = \bar{A}^b h_{t+1}^b + \bar{B}^b x_t \quad (4)$$

$$y_t^b = C^b h_t^b + D^b x_t \quad (5)$$

$$y_t = y_t^f + y_t^b \quad (6)$$

Note that the additional backward scan need to read/write the entire sequence with its parameters and thus expensive. For better distinguishing with our locally bi-direction method, we refer to this scan as *global bi-direction scan*.

3.2 Locally bi-directional SSM architecture

We detail the bi-directional SSM architecture, the key component of LBMamba. In contrast to the global bi-direction scan in figure 1 center that conducts a separate backward scan from the end to the beginning of the sequence, LBMamba conducts a local backward scan within sub-sequences (figure 1 right). This process can be integrated into the forward scan process and thus only requires one time read/write, which saves a lot of time.

As shown in figure 1 right, we first conduct a global forward scan as equation 1. Then we divide the input sequence of length L into sub-sequences which all have a length of M ($M=3$ in the figure). M is set to the number of elements one thread processes and we detail it section 3.4. In each of these sub-sequences, we conduct a backward scan as that in equation 4. Specifically, the state h_t^b obtained during the local backward scan is:

$$h_t^b = \begin{cases} B^f x_t & \text{if } t \% M = 0 \\ \bar{A}^f h_{t+1}^b + \bar{B}^f x_t & \text{otherwise} \end{cases} \quad (7)$$

Since this backward scan is integrated into the forward scan, we have to reuse the same parameters as the forward scan. We then add this backward hidden state and forward hidden state h_t^f . Because the same $B^f x_t$ is added in both forward and backward state in equation 7 and equation 1, we deduct it in the summation. This deduction does not count for computation as we can omit it by a simple programming trick (see Appendix A).

$$h_t = h_t^f + (h_t^b - B^f x_t), \quad y_t = C^f h_t + D^f x_t \quad (8)$$

3.3 Architecture of LBVim

Building upon LBMamba, we introduce the overall architecture of LBVim. LBVim is based on Vim (Zhu et al., 2024). As shown in figure 2, The patch embedding and position embedding follow the same design

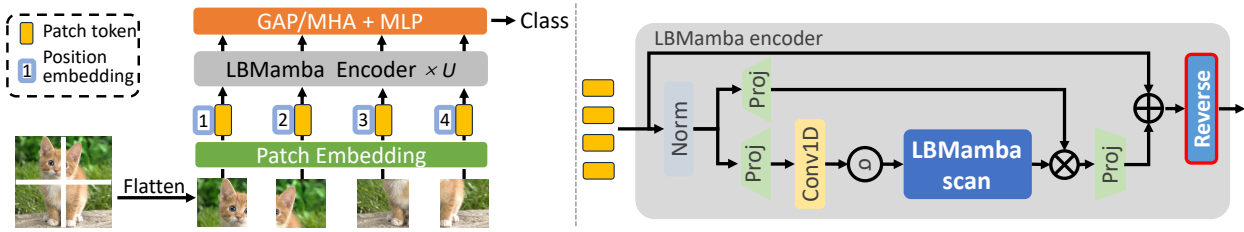


Figure 2: (Left): The overall architecture of LBVim: The input image is split into patches and are embedded as patch tokens. These tokens, combined with positional embeddings, are fed to U LBMamba encoders. Finally, an global average pooling (GAP) layer or a multi-head attention layer (MHA), followed by an MLP head, predicts the image class. (Right): The architecture of LBVim encoder. We reverse the sequence in the end of each encoder such that the global scan direction in LBMamba is switched every two consecutive encoders, ensuring that each token achieves a global receptive field after every two encoders.

as Vim. The embedded patches are then processed by U LBMamba encoders. We replace Vim’s global bi-directional selective scan with our locally bidirectional variant. As LBMamba is not a global bi-directional scan, in one encoder each token does not have a global view of the sequence. To alleviate this problem, we reverse the feature sequence at the end of each encoder to alternate the global scan direction (forward or backward). It allows each token to achieve a global receptive field after every two encoders.

Notably, we does not use the class token commonly used in (Dosovitskiy et al., 2020; Zhu et al., 2024), as it underperforms in our model. Instead, we employ an Global Average Pooling (GAP) layer followed by an MLP for final prediction in small sized models. When the size of the model scales up, we use an Multi-Head Attention with latent query mechanism (MHA) to aggregate features from the last LBMamba encoder:

$$class = MLP(softmax(\frac{qK^T(ft)}{\sqrt{d}}V(ft))) \quad (9)$$

where q is a single learnable token, similar to the class token, ft are the features from the last LBMamba encoder, d is the dimension of features, $K(\cdot), V(\cdot)$ are learnable linear functions and $class$ is the final prediction. Unlike the self attention mechanism, this attention only has one query and thus has linear time complexity. We find that on larger models, MHA achieves better performance than GAP.

3.4 Hardware-aware thread-level bi-directional scanning operator

We present our *hardware-aware scanning operator* that accelerates LBMamba scans. We first revisit the GPU storage hierarchy and then present our novel operator in detail.

GPU storage hierarchy. Figure 3 right illustrates the storage hierarchy of modern GPUs. The green region denotes off-chip GPU memory, with low speed and high capacity. It is referred to as *high bandwidth memory* (HBM). The orange area denotes on-chip static RAM (SRAM), with high speed but low capacity. The blue region highlights the per-thread registers, the fastest tier yet restricted to at most 255 registers per thread. In typical GPU algorithms, data is transferred from HBM to registers for computation, and the results are stored back to HBM to free SRAM and registers for succeeding computation. Because registers are private to each thread, inter-thread communication usually traverse the SRAM, which is substantially more costly than intra-thread computation. Large-scale HBM operations are even more expensive. As a consequence, many GPU algorithms (Dao et al., 2022; Dao, 2024), including Mamba, are bounded not by arithmetic computation but by memory bandwidth.

Mamba’s global forward scan. Figure 3 outlines the vanilla Mamba’s global forward scan algorithm in the blue box. Each GPU thread first fetches a tile of P sequence elements from HBM into its registers ($P = 3$ in the example). The thread then performs an in-register prefix scan over these P elements. We denote the partial result by $h_{i \rightarrow j}$, the hidden state obtained by scanning from time step i to j . To extend the scan across the entire sequence, threads exchange their partial results through **SRAM**. Specifically, thread j acquires a *prefix* that represents the scan of all elements preceding its own tile. For instance, thread T_2 in the figure

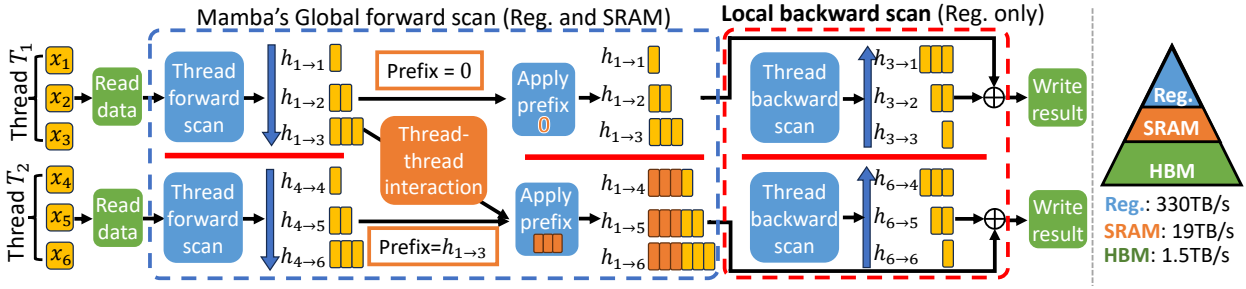


Figure 3: Our hardware-aware LBMMamba CUDA operator with thread-level locally bi-directional scan. Blue color represents operations on registers (Reg.), Orange color represents operations on SRAM and green color represents those on HBM. Blue box shows the scanning operations by the *vanilla Mamba*: two threads T_1 and T_2 first loads 3 elements from HBM to registers. The global forward scan is then conducted as follows: 1) Each thread performs an in-register prefix scan over 3 elements. 2) Threads exchange their partial results through SRAM to get the prefix of each thread. 3) Each thread combines its prefix with its private elements, completing the global scan. Finally, the scanned results are write back to HBM. Red box highlights the **extra** scanning operations by the *LBMMamba*: Each thread performs an in-register backward scan over 3 elements (the same as step 1 except the direction) and add it to the forward scan results. All the extra operations are in registers and thus it is very fast. $h_{i \rightarrow j}$ is the the partial result, the hidden state obtained by scanning from time step i to j .

receives $h_{1 \rightarrow 3}$, the scan of x_1 to x_3 . Because this step requires inter-thread communication, it is significantly more expensive than intra-thread computation. After obtaining the prefix, each thread combines it with its private elements, completing the global scan, and finally writes the results back to HBM. Note that both the local scan and the prefix application traverse the same P elements, doubling the arithmetic cost relative to a purely sequential scan. The conventional bi-directional scan defined by Eq. (4) is very expensive because it executes two full forward scans, thereby incurring twice the HBM traffic and inter-thread communication overhead.

Thread level bi-directional scan. The proposed locally bidirectional scan operator executes the backward scan entirely within each thread, avoiding any extra synchronization. As illustrated in figure 3, we begin with the same global forward scan used in *vanilla Mamba*. Before the results are written back to HBM, each thread performs a second scan over its private tile in the reverse (backward) direction (highlighted by the red box). This backward pass mirrors the thread scan in the forward pass but processes elements in a reversed order. The forward and backward partial sums are then added and streamed to HBM. This backward scan is thread level and does not need to apply prefix, reducing half the computation compared with a global scan. Also, because the backward scan never leaves the registers, it introduces no additional HBM traffic or inter-thread communication and is therefore extremely fast. Although this extra pass increases the overall arithmetic workload by 27%, the running time rises by only 2% (see section 4.2).

4 Experiments

In this section, we present a series of experiments to evaluate the performance of LBVim and compare it mainly to DeiT (Touvron et al., 2021) and Vim (Zhu et al., 2024) across various visual tasks. We also apply LBMMamba to SOTA MIL method MambaMIL and SRMMambaMIL to evaluate its performance on WSI datasets (Yang et al., 2024b). Following Mamba(Gu & Dao, 2023), we set the number of elements each thread thread process (M) based on the sequence length L : when $L > 256$ (images larger than 256×256), a thread processes $M = 16$ elements; for $128 < L \leq 256$ (images between 256×256 and 256×128), it processes $M = 8$ elements; and when $L \leq 128$, the workload is reduced to $M = 4$. All natural image models are trained on 2/4 Nvidia A100/H100 GPUs. All throughput, GPU memory consumption and pathology models are run and evaluated on a Nvidia Quadro RTX 8000 GPU. Other implementation details are in Appendix.

Table 1: Top-1 accuracy (%) and throughput (images/second, denoted as T.P.) of LBVim variants on ImageNet-1K with 224×224 inputs. LBVim-Ti matches Vim-Ti (with global average pooling) while delivering an 82% higher throughput. LBVim-S is only 0.7 percentage points below Vim-S yet runs 69% faster. LBVim-300 and LBVim-528 attain substantially higher accuracy than Vim-Ti and Vim-S, respectively, at comparable throughput.

Method	#Param	FLOPs	T.P.	Top-1 acc%
DeiT-Ti	6M	1.3G	-	72.2
Vim-Ti	7M	1.6G	889	76.1
Vim-Ti (GAP)	7M	1.6G	897	73.9
LBVim-Ti	6M	1.4G	1621	73.7
LBVim-300	15M	3.1G	906	77.7
DeiT-S	22M	4.6G	-	79.8
Vim-S	26M	5.3G	392	80.3
LBVim-S	24M	4.9G	663	79.6
LBVim-528	44M	9.0G	398	81.1

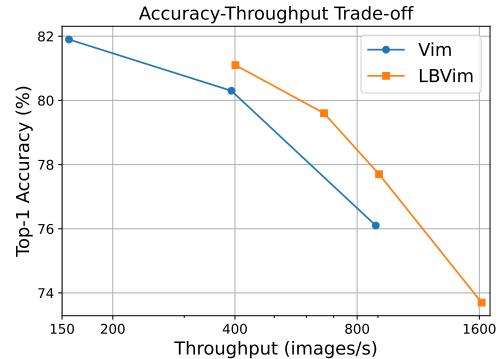


Figure 4: The accuracy-throughput trade-off curve of Vim and LBVim. The curve of LBVim consistently lies in the upper-right quadrant relative to Vim, highlighting a more favorable trade-off. We include the base version of Vim to better illustrate the trends on larger models.

4.1 Natural image classification

We first evaluate LBVim on the ImageNet-1K dataset (Deng et al., 2009), which contains 1.28M training images and 50K validation images from 1,000 categories. All models are trained on the training set, and top-1 accuracy on the validation set is reported. For fair comparisons, we follow the training setting in (Zhu et al., 2024). To be specific, we train our models for 300 epochs using a batch size of 1,024 for tiny model and a batch size of 512 otherwise. We use the AdamW optimizer (Loshchilov & Hutter, 2017) with a momentum of 0.9, a cosine annealing learning with an initial value of 1×10^{-3} , a 5-epoch warmup period and a weight decay of 0.05. For data augmentation, we apply standard techniques: random cropping, horizontal flipping, label-smoothing regularization, mixup, and random erasing.

Table 1 shows our LBVim family with similar sized Vim baselines. At the tiny scale (192 feature dimension), with out a global backward scan, LBVim-Ti delivers a 82% higher throughput than Vim-Ti and while using 1 M fewer parameters. The top-1 accuracy trails Vim-T by 2.4%, which we attribute to the current inability of our architecture to process the class token. Comparing with Vim-Ti with global average pooling, our method achieves comparable performance (only 0.2% lower). Moving to the small setting (384 feature dimension), the accuracy gap narrows to 0.7% as the model capacity increases, yet throughput remains markedly (69%) higher.

Compared with Vim, LBVim has better speed-accuracy trade-off. We introduce two intermediate model configurations, LBVim-300 and LBVim-528. Where 300 and 528 are the dimension of features. As shown in table 1, their throughput closely match those of Vim-T and Vim-S, but surpassing the corresponding baselines by 1.6% and 0.8% in accuracy, respectively. As illustrated in figure 4, the accuracy-throughput curve of our models consistently lies in the upper-right quadrant relative to Vim, highlighting a more favorable trade-off across a wide operating range. These findings also show that instead of conducting an additional backward scan, it is better to spend the running time on larger model dimensions.

4.2 FLOPs and speed analysis

Although LBMamba performs significant additional computations compared to vanilla Mamba, it maintains fast processing speeds. At the CUDA-kernel level (table 2), LBMamba kernel executes 27% more floating-point operations than the vanilla Mamba kernel for all tested resolutions. Despite this arithmetic inflation, throughput drops by only 1.9–2.3% across all tested resolutions and the GPU memory consumption remains unchanged. The minimal slowdown stems from the fact that the extra computations are confined to on-

Table 2: Comparison of floating-point operations per image (FLOPs), throughput (T.P., images or feature maps per second), and GPU memory consumption (Mem.) during inference with a batch size of 128. Input images are preloaded to GPU. For a fair comparison, we use global average pooling for Vim-Ti.

Image size Method	256 × 256			512 × 512			1024 × 1024		
	FLOPs	T.P.	Mem.	FLOPs	T.P.	Mem.	FLOPs	T.P.	Mem.
Mamba CUDA kernel	17M	87.4K	209M	69M	14.3K	827M	277M	3.8K	3.3G
LBMamba CUDA kernel	22M	85.4K	209M	88M	14.0K	827M	352M	3.7K	3.3G
Vim-Ti	2.1G	795	755M	8.3G	162	2.9G	33.4G	42	11.0G
LBVim-Ti	1.9G	1421	608M	7.4G	296	2.2G	29.6G	77	8.6G
LBVim-300	4.1G	799	862M	16.4G	169	3.4G	65.4G	47	12.6G

chip registers, incur no thread-thread interaction, and bypass the HBM or SRAM traffic. Zooming out to the model, LBVim-Ti, leveraging the LBMambakernel and omits the additional scan operation required by Vim-Ti, achieves 79%-83% higher throughput, accompanied with a 19-22% reduction in GPU memory. LBVim-300 has nearly doubled FLOPs compared with Vim-Ti but is as fast as Vim-Ti. It achieves superior performance (section 4.1) with only 14-17% additional GPU memory. This confirms that LBVim delivers a superior efficiency without sacrificing scalability. We show that this superior efficiency scale to training as well (see Appendix B)

4.3 Downstream tasks on natural images

We evaluate the performance of LBVim on downstream tasks, including semantic segmentation on ADE20K dataset (Zhou et al., 2019), and object detection and instance segmentation on the COCO 2017 dataset (Lin et al., 2014). The training framework is based on the MMSegmenation (Contributors, 2020) and MMDection (Chen et al., 2019) libraries, following (Zhu et al., 2024) in utilizing UperNet (Xiao et al., 2018) and Cascade Mask R-CNN (Cai & Vasconcelos, 2019) as the segmentation and detection networks, respectively. For a fair comparison, we add Linear layers to LBVim-300 and LBVim-528, adjusting their output dimension to be the same as Vim-Ti and Vim-S, respectively. We find that for these two downstream tasks, which operates on dense features and therefore does not rely on a dedicated class token, the performance gap between LBVim and the Vim baseline narrows markedly.

Semantic Segmentation. Table 3 left presents the mIoU results on the ADE20K dataset. The lightweight LBVim-Ti reaches 40.2 mIoU, only 0.8% below its Vim-Ti counterpart, while LBVim-S attains 44.2 mIoU, trailing Vim-S by 0.7%. When we modestly increase capacity to match Vim throughput, the gains become pronounced: LBVim-300 achieves 43.7 mIoU, 2.7 % above Vim-Ti. Similarly, LBVim-528 pushes the score to 45.5 mIoU, surpassing Vim-S by 0.6%.

Object Detection and Instance Segmentation. Table 3 right reports the average precision results the COCO 2017 dataset. For box AP (AP^b), LBVim-Ti attains 45.4%, which is on par with Vim-Ti (45.7%) and 1.1% above DeiT-Ti. Mask accuracy (AP^m) follows the same trend: LBVim-Ti matches Vim-Ti at 39.2% and outperforms the DeiT baseline by 1.1%. As to LBVim-300, which has similar through put as Vim-Ti, achieves 0.9% higher AP^b and 1.1% higher AP^m . These results on segmentation and detection further demonstrate that LBVimdelivers a more favorable accuracy-efficiency trade-off on downstream tasks.

4.4 Ablation study

We ablate the two principal designs in LBVim—the LBMambakernel and the sequence reversing operation on the ImageNet-1K classification dataset. Table 4 shows that removing the LBMamba kernel (w.o. LBMamba) lowers accuracy by 1% with negligible impact (0.4%) on throughput. The drop confirms that the locally backward scan embedded in LBMamba improves feature propagation. On the other hand, eliminating sequence reversing operation (w.o. sequence reverse) results in a larger accuracy degradation of 4.5%. The sequence reversing operation alternates the scan direction of LBVim layers, granting each token a global

Table 3: **Left:** The performance of our LBVim on the ADE20K semantic segmentation dataset. FLOPs and throughput (T.P.) are measured with an input size of 512×2048 . **Right:** The performance of LBVim on the COCO detection dataset (image are of size 1024×1024). AP^b and AP^m denote the average precision for bonding boxes and masks, respectively. T.P. denotes average throughput.

Backbone	#Param.	FLOPs	T.P.	mIoU	Backbone	#Param.	AP^b	AP_{50}^b	AP_{75}^b	AP_{50}^b	AP_m^b	AP_l^b
DeiT-Ti	11M	-	-	39.2	DeiT-Ti	-	44.4	63.0	47.8	26.1	47.4	61.8
Vim-Ti	13M	145G	25	41.0	Vim-Ti	66M	45.7	63.9	49.6	26.1	49.0	63.2
LBVim-Ti	12M	141G	35	40.2	LBVim-Ti	66M	45.4	63.8	49.3	25.5	49.4	62.4
LBVim-300	21M	178G	26	43.7	LBVim-300	74M	46.6	65.2	50.5	27.0	50.6	63.6
DeiT-S	43M	-	-	41.0	Backbone	T.P.	AP^m	AP_{50}^m	AP_{75}^m	AP_{50}^m	AP_m^m	AP_l^m
Vim-S	46M	227G	15	44.9	DeiT-Ti	-	38.1	59.9	40.5	18.1	40.5	58.4
LBVim-S	44M	219G	21	44.2	Vim-T	7.3	39.2	60.9	41.7	18.2	41.8	60.2
LBVim-528	65M	306G	15	45.5	LBVim-Ti	7.7	39.2	60.9	41.8	17.9	42.1	60.0
					LBVim-300	7.3	40.3	62.5	43.1	19.3	43.5	60.4

Table 4: **Left:** The ablation study of LB-Mamba and the sequence reserving operation in LBVim on the ImageNet-1k classification dataset. **Right:** Ablation of global average pooling (GAP) vs. multi-head attention pooling (MAP) in LBVim on the ImageNet-1k classification dataset. T.P. denotes inference throughput (images/second).

Method	T.P.	Top-1 Acc%
LBVim-T	1621	73.7
w.o. LB-Mamba	1628	72.7
w.o. sequence reverse	1711	69.2

Model	GAP		MAP	
	T.P.	Acc%	T.P.	Acc%
LBVim-Ti	1621	73.7	1610	73.0
LBVim-300	906	77.7	901	77.3
LBVim-S	663	79.6	658	79.4
LBVim-528	401	80.0	398	81.1

receptive field every two layers, and thus strengthening long-range context modeling. Without this global receptive field, the performance drop dramatically.

We also conduct an ablation on the output aggregation scheme: global average pooling (GAP) versus multi-head attention pooling (MAP), across four capacity levels of LBVim in table 4 right. For the tiny, 300 and small variants, GAP delivers a 0.7%, 0.4% and 0.2% higher top-1 accuracy, respectively. It is clear that when the model scales up in dimension, the advantage of GAP narrows. When the model scales to LBVim-528, the MAP gains 1.1% at a negligible 0.7 % slowdown over GAP, indicating that the expressive benefit of learned pooling emerges only when sufficient parameters are available. This size-dependent trend aligns with prior observations that simple pooling is preferable for some compact models (Pan et al., 2021), whereas attention-based aggregation becomes advantageous in larger models (Dosovitskiy et al., 2020).

4.5 WSI classification

To verify LB-Mamba beyond natural images, we embed it into the SOTA Multiple-Instance Learning (MIL) framework, MambaMIL and SRMambaMIL (Yang et al., 2024b), and name them LB-MambaMIL and SRLB-MambaMIL, respectively. We evaluate them on 3 public available Whole Slide Image datasets, PANDA (prostate grade assessment) (Bulten et al., 2022), TCGA-NSCLC (adenocarcinoma vs. squamous lung cancer) and TCGA-BRCA (breast invasive carcinoma sub-typing) (tcg). Dataset and training details are listed in Appendix D and E. As shown in table 5, with an additional locally backward scan, LB-MambaMIL generally performs better than MambaMIL, achieves up to 3.06% higher accuracy, up to 3.39% higher F1 and up to 1.67% higher AUC. Similar improvement is also observed on SRMamba, SRLB-MambaMIL achieves up to 2.98% higher accuracy, up to 2.90% higher F1 and up to 1.48% higher AUC, demonstrating

Table 5: The comparison of accuracy (Acc), F1 and AUC on five WSI classification datasets. We conducted each experiment five times using five different random seeds and reported their mean. The highest metrics are marked as **bold**.

Method	PANDA			TCGA-NSCLC			TCGA-BRCA		
	Acc	F1	AUC	Acc	F1	AUC	Acc	F1	AUC
AB-MIL	0.4883	0.4269	0.7797	0.8758	0.8756	0.9572	0.9292	0.8893	0.9747
DSMIL	0.4633	0.3847	0.7660	0.8782	0.8780	0.9567	0.9375	0.8961	0.9770
CLAM	0.4802	0.4224	0.7820	0.8804	0.8803	0.9536	0.9333	0.8960	0.9753
DTFD-MIL	0.4704	0.3853	0.7665	0.8736	0.8732	0.9559	0.9271	0.8809	0.9633
TransMIL	0.4636	0.3970	0.7728	0.8850	0.8845	0.9626	0.9375	0.9028	0.9763
MambaMIL	0.4679	0.4216	0.7781	0.8758	0.8756	0.9582	0.9333	0.8939	0.9657
LBMambaMIL	0.4985	0.4499	0.7948	0.8874	0.8870	0.9582	0.9333	0.9015	0.9673
SRMambaMIL	0.4711	0.4209	0.7776	0.8850	0.8849	0.9592	0.9313	0.8900	0.9657
SRLBMMambaMIL	0.5009	0.4499	0.7924	0.9035	0.9032	0.9619	0.9375	0.9042	0.9681

that the LBMamba is able to improve the performance of unidirectional scans. It also shows that our method generalize well on Giga-pixel pathology images.

4.6 Visualization of Effective Receptive Fields.

The Effective Receptive Field (ERF) (Luo et al., 2016) refers to the region in the input space that contributes to the activation of a specific output unit. We conduct a comparative analysis of the central pixel’s ERF on DeiT, Vim and LBVim at tiny and small scale, both before and after training. The results presented in figure 5 illustrate that DeiT shows global ERFs but it suffers from the quadratic complexity of self attention. Vim shows global ERFs and LBVim also shows global ERFs, proving that LBMamba with sequence reversing operation does not have a side effect on ERF.

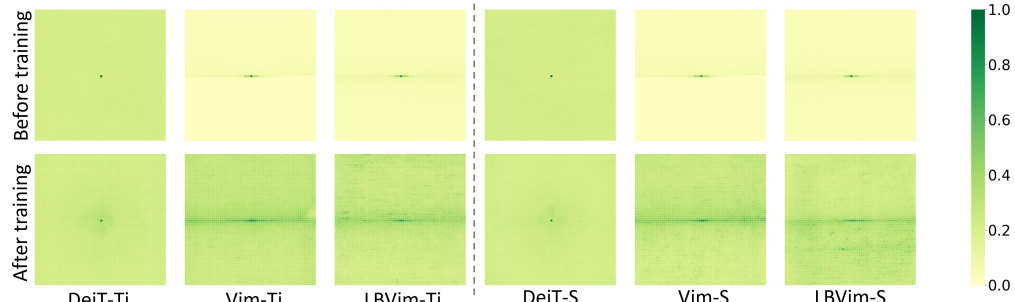


Figure 5: Comparison of Effective Receptive Fields (ERF) (Luo et al., 2016) on DeiT, Vim and LBVim at tiny and small scale. Pixels with higher intensity indicate larger responses related to the central pixel.

5 Conclusion

We proposed **LBMamba**, a thread-level bi-directional state-space module that marries the linear complexity of Mamba with a register-resident local backward scan. The resulting **LBVim** backbone dispenses with costly global reverse passes yet still attains a full receptive field by alternating scan directions across consecutive layers. Extensive experiments on four diverse vision tasks confirm three key findings: *Efficiency*: LBMamba adds negligible runtime overhead (2%) while eliminating one full sweep, translating to up to 83% higher throughput. *Accuracy*: Under equal or lower latency budgets, LBVim surpasses Vim by up to 1.6% ImageNet top-1 accuracy, 2.7% mIoU on ADE20K, 0.9% AP^b and 1.1% AP^m gains on COCO, 1.67% in AUC gains on WSI benchmarks. *Scalability*: When the size of model scales up, the accuracy–throughput Pareto

front consistently dominates global bi-directional baselines, showing a better accuracy-throughput trade-off. Together, these advances indicate that local bi-directionality plus sequence reversing operation is sufficient for strong global context modeling while preserving the hallmark efficiency of SSMs.

Limitation. LBMamba is less effective when a dedicated class token is appended to the sequence. We systematically evaluated four common variants: head class token (prepended), middle class token (inserted at the sequence midpoint), and double class token (both prepended and appended) strategy, but none of them achieves better performance than a simple global average pooling (see Appendix C). A plausible explanation is that the *local backward scan* treats the class token as an ordinary feature vector whose receptive field is confined to its local window; this reinforces local patterns while diluting the holistic summary that the token is meant to capture. Unifying local bi-directionality with an effective global summarization mechanism therefore remains an open research question, and we leave a deeper investigation of this to future work.

References

The Cancer Genome Atlas Program (TCGA) — cancer.gov. <https://www.cancer.gov/ccg/research/genome-sequencing/tcga>.

Ethan Baron, Itamar Zimerman, and Lior Wolf. 2-d ssm: A general spatial layer for visual transformers. *arXiv preprint arXiv:2306.06635*, 2023.

Wouter Bulten, Kimmo Kartasalo, Po-Hsuan Cameron Chen, Peter Ström, Hans Pinckaers, Kunal Nagpal, Yuannan Cai, David F Steiner, Hester Van Boven, Robert Vink, et al. Artificial intelligence for diagnosis and gleason grading of prostate cancer: the panda challenge. *Nature medicine*, 28(1):154–163, 2022.

Zhaowei Cai and Nuno Vasconcelos. Cascade r-cnn: High quality object detection and instance segmentation. *IEEE transactions on pattern analysis and machine intelligence*, 43(5):1483–1498, 2019.

Kai Chen, Jiaqi Wang, Jiangmiao Pang, Yuhang Cao, Yu Xiong, Xiaoxiao Li, Shuyang Sun, Wansen Feng, Ziwei Liu, Jiarui Xu, Zheng Zhang, Dazhi Cheng, Chenchen Zhu, Tianheng Cheng, Qijie Zhao, Buyu Li, Xin Lu, Rui Zhu, Yue Wu, Jifeng Dai, Jingdong Wang, Jianping Shi, Wanli Ouyang, Chen Change Loy, and Dahua Lin. MMDetection: Open mmlab detection toolbox and benchmark. *arXiv preprint arXiv:1906.07155*, 2019.

Richard J Chen, Chengkuan Chen, Yicong Li, Tiffany Y Chen, Andrew D Trister, Rahul G Krishnan, and Faisal Mahmood. Scaling vision transformers to gigapixel images via hierarchical self-supervised learning. In *Proceedings of the IEEE/CVF conference on computer vision and pattern recognition*, pp. 16144–16155, 2022.

Richard J Chen, Tong Ding, Ming Y Lu, Drew FK Williamson, Guillaume Jaume, Bowen Chen, Andrew Zhang, Daniel Shao, Andrew H Song, Muhammad Shaban, et al. Towards a general-purpose foundation model for computational pathology. *Nature Medicine*, 2024.

MMSegmentation Contributors. MMSegmentation: Openmmlab semantic segmentation toolbox and benchmark. <https://github.com/open-mmlab/mmsegmentation>, 2020.

Tri Dao. FlashAttention-2: Faster attention with better parallelism and work partitioning. In *International Conference on Learning Representations (ICLR)*, 2024.

Tri Dao, Daniel Y. Fu, Stefano Ermon, Atri Rudra, and Christopher Ré. FlashAttention: Fast and memory-efficient exact attention with IO-awareness. In *Advances in Neural Information Processing Systems (NeurIPS)*, 2022.

Jia Deng, Wei Dong, Richard Socher, Li-Jia Li, Kai Li, and Li Fei-Fei. Imagenet: A large-scale hierarchical image database. In *2009 IEEE conference on computer vision and pattern recognition*, pp. 248–255. Ieee, 2009.

Jacob Devlin, Ming-Wei Chang, Kenton Lee, and Kristina Toutanova. Bert: Pre-training of deep bidirectional transformers for language understanding. In *Proceedings of the 2019 conference of the North American chapter of the association for computational linguistics: human language technologies, volume 1 (long and short papers)*, pp. 4171–4186, 2019.

Alexey Dosovitskiy, Lucas Beyer, Alexander Kolesnikov, Dirk Weissenborn, Xiaohua Zhai, Thomas Unterthiner, Mostafa Dehghani, Matthias Minderer, Georg Heigold, Sylvain Gelly, et al. An image is worth 16x16 words: Transformers for image recognition at scale. *arXiv preprint arXiv:2010.11929*, 2020.

Leo Filliou, Joseph Boyd, Maria Vakalopoulou, Paul-Henry Cournède, and Stergios Christodoulidis. Structured state space models for multiple instance learning in digital pathology. In *International Conference on Medical Image Computing and Computer-Assisted Intervention*, pp. 594–604. Springer, 2023.

Albert Gu and Tri Dao. Mamba: Linear-time sequence modeling with selective state spaces. *arXiv preprint arXiv:2312.00752*, 2023.

Albert Gu, Karan Goel, and Christopher Ré. Efficiently modeling long sequences with structured state spaces. *arXiv preprint arXiv:2111.00396*, 2021a.

Albert Gu, Isys Johnson, Karan Goel, Khaled Saab, Tri Dao, Atri Rudra, and Christopher Ré. Combining recurrent, convolutional, and continuous-time models with linear state space layers. *Advances in neural information processing systems*, 34:572–585, 2021b.

Tao Huang, Xiaohuan Pei, Shan You, Fei Wang, Chen Qian, and Chang Xu. Localmamba: Visual state space model with windowed selective scan. *arXiv preprint arXiv:2403.09338*, 2024.

Sukjun Hwang, Aakash Sunil Lahoti, Ratish Puduppully, Tri Dao, and Albert Gu. Hydra: Bidirectional state space models through generalized matrix mixers. *Advances in Neural Information Processing Systems*, 37: 110876–110908, 2024.

Maximilian Ilse, Jakub Tomczak, and Max Welling. Attention-based deep multiple instance learning. In *International conference on machine learning*, pp. 2127–2136. PMLR, 2018.

Rudolph Emil Kalman. A new approach to linear filtering and prediction problems. 1960.

Sun-Yuan Kung, Bernard C Levy, Martin Morf, and Thomas Kailath. New results in 2-d systems theory, part ii: 2-d state-space models—realization and the notions of controllability, observability, and minimality. *Proceedings of the IEEE*, 65(6):945–961, 1977.

Bin Li, Yin Li, and Kevin W Eliceiri. Dual-stream multiple instance learning network for whole slide image classification with self-supervised contrastive learning. In *Proceedings of the IEEE/CVF Conference on Computer Vision and Pattern Recognition*, pp. 14318–14328, 2021.

Tsung-Yi Lin, Michael Maire, Serge Belongie, James Hays, Pietro Perona, Deva Ramanan, Piotr Dollár, and C Lawrence Zitnick. Microsoft coco: Common objects in context. In *Computer vision–ECCV 2014: 13th European conference, zurich, Switzerland, September 6–12, 2014, proceedings, part v 13*, pp. 740–755. Springer, 2014.

Yue Liu, Yunjie Tian, Yuzhong Zhao, Hongtian Yu, Lingxi Xie, Yaowei Wang, Qixiang Ye, Jianbin Jiao, and Yunfan Liu. Vmamba: Visual state space model. *Advances in neural information processing systems*, 37: 103031–103063, 2024.

Ilya Loshchilov and Frank Hutter. Decoupled weight decay regularization. *arXiv preprint arXiv:1711.05101*, 2017.

Ming Y Lu, Drew FK Williamson, Tiffany Y Chen, Richard J Chen, Matteo Barbieri, and Faisal Mahmood. Data-efficient and weakly supervised computational pathology on whole-slide images. *Nature Biomedical Engineering*, 5(6):555–570, 2021.

Wenjie Luo, Yujia Li, Raquel Urtasun, and Richard Zemel. Understanding the effective receptive field in deep convolutional neural networks. *Advances in neural information processing systems*, 29, 2016.

Eric Nguyen, Karan Goel, Albert Gu, Gordon Downs, Preey Shah, Tri Dao, Stephen Baccus, and Christopher Ré. S4nd: Modeling images and videos as multidimensional signals with state spaces. *Advances in neural information processing systems*, 35:2846–2861, 2022.

Maxime Oquab, Timothée Darcet, Théo Moutakanni, Huy Vo, Marc Szafraniec, Vasil Khalidov, Pierre Fernandez, Daniel Haziza, Francisco Massa, Alaaeldin El-Nouby, et al. Dinov2: Learning robust visual features without supervision. *arXiv preprint arXiv:2304.07193*, 2023.

Zizheng Pan, Bohan Zhuang, Jing Liu, Haoyu He, and Jianfei Cai. Scalable vision transformers with hierarchical pooling. In *Proceedings of the IEEE/cvf international conference on computer vision*, pp. 377–386, 2021.

Zhuchen Shao, Hao Bian, Yang Chen, Yifeng Wang, Jian Zhang, Xiangyang Ji, et al. Transmil: Transformer based correlated multiple instance learning for whole slide image classification. *Advances in neural information processing systems*, 34:2136–2147, 2021.

Hugo Touvron, Matthieu Cord, Matthijs Douze, Francisco Massa, Alexandre Sablayrolles, and Hervé Jégou. Training data-efficient image transformers & distillation through attention. In *International conference on machine learning*, pp. 10347–10357. PMLR, 2021.

Chengkun Wang, Wenzhao Zheng, Yuanhui Huang, Jie Zhou, and Jiwen Lu. V2m: Visual 2-dimensional mamba for image representation learning. *arXiv preprint arXiv:2410.10382*, 2024.

Junxiong Wang, Jing Nathan Yan, Albert Gu, and Alexander M Rush. Pretraining without attention. *arXiv preprint arXiv:2212.10544*, 2022.

Tete Xiao, Yingcheng Liu, Bolei Zhou, Yuning Jiang, and Jian Sun. Unified perceptual parsing for scene understanding. In *Proceedings of the European conference on computer vision (ECCV)*, pp. 418–434, 2018.

Chenhongyi Yang, Zehui Chen, Miguel Espinosa, Linus Ericsson, Zhenyu Wang, Jiaming Liu, and Elliot J Crowley. Plainmamba: Improving non-hierarchical mamba in visual recognition. *arXiv preprint arXiv:2403.17695*, 2024a.

Shu Yang, Yihui Wang, and Hao Chen. Mambamil: Enhancing long sequence modeling with sequence reordering in computational pathology. In *International Conference on Medical Image Computing and Computer-Assisted Intervention*, pp. 296–306. Springer, 2024b.

Jingwei Zhang, Anh Tien Nguyen, Xi Han, Vincent Quoc-Huy Trinh, Hong Qin, Dimitris Samaras, and Mahdi S Hosseini. 2dmamba: Efficient state space model for image representation with applications on giga-pixel whole slide image classification. *arXiv preprint arXiv:2412.00678*, 2024.

Bolei Zhou, Hang Zhao, Xavier Puig, Tete Xiao, Sanja Fidler, Adela Barriuso, and Antonio Torralba. Semantic understanding of scenes through the ade20k dataset. *International Journal of Computer Vision*, 127:302–321, 2019.

Lianghui Zhu, Bencheng Liao, Qian Zhang, Xinlong Wang, Wenyu Liu, and Xinggang Wang. Vision mamba: Efficient visual representation learning with bidirectional state space model. In *Forty-first International Conference on Machine Learning*, 2024.

A LBVim block algorithm

Algorithm 1 shows the algorithm of LBVim block, where token sequence \mathbf{T}_{l-1} is the the input and token sequence \mathbf{T}_l^{rev} is the reversed output, l denotes the layer number. Line 22 to 31 is our locally backward operation corresponds to equation 7 and equation 8. The simple programming trick to avoid subtracting Bx we mentioned in section 3.2 is on line where we do not add Bx when initially when calculating $h^{backward}$ and use this result to calculate y . When this is finished, we then add Bx back on line such that when moving to the next time step, the calculation is correct. Line 36 represents the sequence reversing operation we mentioned in section 3.3 and figure 2.

Algorithm 1 LBVim Block Process

Require: token sequence $\mathbf{T}_{l-1} : (\mathbf{B}, \mathbf{L}, \mathbf{D})$
Ensure: reversed token sequence $\mathbf{T}_l^{rev} : (\mathbf{B}, \mathbf{L}, \mathbf{D})$

- 1: /* normalize the input sequence \mathbf{T}_{l-1}' */
- 2: $\mathbf{T}_{l-1}' : (\mathbf{B}, \mathbf{L}, \mathbf{D}) \leftarrow \mathbf{Norm}(\mathbf{T}_{l-1})$
- 3: $\mathbf{x} : (\mathbf{B}, \mathbf{L}, \mathbf{E}) \leftarrow \mathbf{Linear}^x(\mathbf{T}_{l-1}')$
- 4: $\mathbf{z} : (\mathbf{B}, \mathbf{L}, \mathbf{E}) \leftarrow \mathbf{Linear}^z(\mathbf{T}_{l-1}')$
- 5: /* Pre-scan processes */
- 6: $\mathbf{x}' : (\mathbf{B}, \mathbf{L}, \mathbf{E}) \leftarrow \mathbf{SiLU}(\mathbf{Conv1d}_o(\mathbf{x}))$
- 7: $\mathbf{B} : (\mathbf{B}, \mathbf{L}, \mathbf{N}) \leftarrow \mathbf{Linear}^B(\mathbf{x}'_o)$
- 8: $\mathbf{C} : (\mathbf{B}, \mathbf{L}, \mathbf{N}) \leftarrow \mathbf{Linear}^C_o(\mathbf{x}')$
- 9: /* softplus ensures positive Δ_o */
- 10: $\mathbf{\Delta} : (\mathbf{B}, \mathbf{L}, \mathbf{E}) \leftarrow \log(1 + \exp(\mathbf{Linear}^\Delta(\mathbf{x}') + \mathbf{Parameter}^\Delta))$
- 11: /* shape of $\mathbf{Parameter}^A$ is (\mathbf{E}, \mathbf{N}) */
- 12: $\mathbf{A} : (\mathbf{B}, \mathbf{L}, \mathbf{E}, \mathbf{N}) \leftarrow \mathbf{\Delta} \otimes \mathbf{Parameter}^A$
- 13: $\overline{\mathbf{B}} : (\mathbf{B}, \mathbf{L}, \mathbf{E}, \mathbf{N}) \leftarrow \mathbf{\Delta} \otimes \mathbf{B}$
- 14: /* initialization with 0 */
- 15: $h^f : (\mathbf{B}, \mathbf{E}, \mathbf{N}) \leftarrow \text{zeros}(\mathbf{B}, \mathbf{E}, \mathbf{N})$
- 16: $h^b : (\mathbf{B}, \mathbf{E}, \mathbf{N}) \leftarrow \text{zeros}(\mathbf{B}, \mathbf{E}, \mathbf{N})$
- 17: $\mathbf{y} : (\mathbf{B}, \mathbf{L}, \mathbf{E}) \leftarrow \text{zeros}(\mathbf{B}, \mathbf{L}, \mathbf{E})$
- 18: /* SSM forward recurrent */
- 19: **for** i in $\{0, \dots, L-1\}$ **do**
- 20: $h^f = \overline{\mathbf{A}}[:, i, :, :] \odot h^f + \overline{\mathbf{B}}[:, i, :, :] \odot \mathbf{x}'[:, i, :, \mathbf{None}]$
- 21: **end for**
- 22: /* Locally backward recurrent */
- 23: **for** i in $\{L-1, \dots, 0\}$ **do**
- 24: **if** $(i+1)\%M == 0$ **then**
- 25: $h^b = 0$
- 26: **else**
- 27: $h^b = \overline{\mathbf{A}}_o[:, i, :, :] \odot h^b$
- 28: **end if**
- 29: $\mathbf{y}[:, i, :] = (h^f + h^b) \otimes \mathbf{C}[:, i, :] + \mathbf{Parameter}^D \otimes \mathbf{x}'[:, i, :]$
- 30: $h^b = h^b + \overline{\mathbf{B}}[:, i, :, :] \odot \mathbf{x}'[:, i, :, \mathbf{None}]$
- 31: **end for**
- 32: /* get gated y */
- 33: $\mathbf{y}' : (\mathbf{B}, \mathbf{L}, \mathbf{E}) \leftarrow \mathbf{y} \odot \mathbf{SiLU}(\mathbf{z})$
- 34: /* residual connection */
- 35: $\mathbf{T}_l : (\mathbf{B}, \mathbf{L}, \mathbf{D}) \leftarrow \mathbf{Linear}^T(\mathbf{y}') + \mathbf{T}_{l-1}$
- 36: $\mathbf{T}_l^{rev} : (\mathbf{B}, \mathbf{L}, \mathbf{D}) \leftarrow \mathbf{Reverse}(\mathbf{T}_l)$
- 37: Return: \mathbf{T}_l^{rev}

B Throughput during training

Table 6 benchmarks training throughput for both the CUDA operator and the complete backbone under a batch size of 32. Similar to the findings in section 4.2, on CUDA kernel level, LBMamba is still only 2-3% slower than the vanilla Mamba kernel, showing that the thread-level bi-directional scan remains efficient

during training. Zooming to the model level, compared with Vim-Ti, LBVim-Ti remains 72-75% faster during training with nearly half of the GPU memory consumption, across all tested resolution. An interesting finding is that LBVim-300 requires 16–18% less GPU memory than Vim-Ti, given that they have similar throughput. This is probably because the standard bi-directional scan need to save more intermediate variables and thus requires more GPU memory during training. These experiments further demonstrate the superior efficiency of LBVim.

Table 6: Comparison of throughput (T.P., images or feature maps per second), and GPU memory consumption (Mem.) during training with a batch size of 32. Input images are preloaded to GPU. For a fair comparison, we use global average pooling for Vim-Ti.

Image size Method	256 × 256		512 × 512		1024 × 1024	
	T.P.	Mem.	T.P.	Mem.	T.P.	Mem.
Mamba CUDA kernel	19.1K	-	2.4K	-	1.0K	-
LBMamba CUDA kernel	18.6K	-	2.4K	-	1.0K	-
Vim-Ti	229	2.7G	53	10.4G	12	41.1G
LBVim-Ti	394	1.5G	93	5.5G	21	21.9G
LBVim-300	224	2.3G	52	8.6G	11	33.8G

C Ablation on the class token

Table 7 shows several common strategies (Zhu et al., 2024) for incorporating a class token into LBVim-Ti on the **ImageNet-100** dataset. Consistent with our observations on ImageNet-1K (section 4.1), LBVim-Ti under performs Vim-Ti by 0.42% as it can not process the class token. Introducing a *head* class token, which is prepended to the patch sequence (ViT style (Dosovitskiy et al., 2020)), reduces accuracy by 3.22%. Adding a second *tail* token (*double* class token) offers a recovery (0.58%) but remains 2.64% lower than GAP. Placing the token in the *middle* (the strategy used by Zhu et al. (2024)) of the sequence partially alleviates the degradation, yet it still under performs the no-token design. We believe this is because the class token is treated as an ordinary feature vector, its ability to aggregate global context is diluted, leading to weaker final representations. In contrast, GAP aggregates information from all positions without introducing additional parameters or disrupting the scan pattern, making it a more compatible summarization mechanism for LBVim-300.

Table 7: Ablation study on common types of class token on the **ImageNet-100** dataset

Class token type	Top-1 Acc%
Vim-Ti	82.66
LBVim-Ti (GAP)	82.24
w. head class token	79.02
w. double class token	79.60
w. middle class token	81.04

D Implementation details of WSI experiments

SSM models For a fair comparison, we use a single SSM-based block with a 128-dimensional SSM and set the state dimension to 16 for all Mamba-based methods.

Feature extractor. We use UNI (Chen et al., 2024), a well-known and current SOTA foundation model for feature extraction, which is a ViT-L/16 pretrained on more than 100 million pathology patches from over 100,000 H&E-stained WSIs across 20 major tissue types. UNI is pretrained in a self-supervised manner using DINOv2 (Oquab et al., 2023).

WSI pre-processing. We extract patches from WSIs at 20x magnification with no overlapping. The patch size is set to 512x512 pixels. We used the preprocessing tool in CLAM (Lu et al., 2021) to segment and extract tissue regions.

Training. We use AdamW (Loshchilov & Hutter, 2017) to optimize the models for 20 epochs of training with batch size being 1. The initial learning rate is 0.0001 and we use cosine annealing decay to adjust it.

E Details of WSI datasets

Prostate cancer grading based on PANDA. Panda dataset (Bulten et al., 2022) consists of 10,614 biopsies of prostate cancer. Its labels are their ISUP grading, totally 6 categories: *grade 0* (2890 slides), *grade 1* (2666 slides), *grade 2* (1343 slides), *grade 3* (1242 slides), *grade 4* (1249 slides), and *grade 5* (1224 slides). We random split PANDA into 80:10:10 train/validation/test sets.

Breast invasive carcinoma subtyping on TCGA-BRCA. TCGA-BRCA comprise 1033 H&E WSIs with 2 subtypes: *invasive ductal carcinoma* (822 slides) and *invasive lobular carcinoma* (211 slides). We follow (Chen et al., 2022) to get the train/validation/test set with 841:96:96 slides.

Non-small cell lung carcinoma subtyping on TCGA-NSCLC. The dataset include 957 H&E breast carcinoma WSIs, including 2 subtypes: *lung adenocarcinoma* (490 slides) and *lung squamous cell carcinoma* (468 slides). We follow (Chen et al., 2022) to split the dataset into train/validation/test set with 785:86:87 slides.